



저작자표시-비영리-변경금지 2.0 대한민국

이용자는 아래의 조건을 따르는 경우에 한하여 자유롭게

- 이 저작물을 복제, 배포, 전송, 전시, 공연 및 방송할 수 있습니다.

다음과 같은 조건을 따라야 합니다:



저작자표시. 귀하는 원저작자를 표시하여야 합니다.



비영리. 귀하는 이 저작물을 영리 목적으로 이용할 수 없습니다.



변경금지. 귀하는 이 저작물을 개작, 변형 또는 가공할 수 없습니다.

- 귀하는, 이 저작물의 재이용이나 배포의 경우, 이 저작물에 적용된 이용허락조건을 명확하게 나타내어야 합니다.
- 저작권자로부터 별도의 허가를 받으면 이러한 조건들은 적용되지 않습니다.

저작권법에 따른 이용자의 권리는 위의 내용에 의하여 영향을 받지 않습니다.

이것은 [이용허락규약\(Legal Code\)](#)을 이해하기 쉽게 요약한 것입니다.

[Disclaimer](#)

Thesis for the Degree of Master of Engineering

Defective UiO-66 induced PVA-based
Mixed Matrix Membrane (MMMs) for
High-Performance water/IPA Separation
through Pervaporation

By

Gyeong Min Choi

Department of Applied Chemical Engineering
(Major of Industrial Chemistry)

The Graduate School

Pukyong National University

February, 2025

Defective UiO-66 induced PVA-based
Mixed Matrix Membrane (MMMs) for
High-Performance water/IPA Separation
through Pervaporation

(결함이 있는 UiO-66 을 도입한 PVA 기반
혼합 매트릭스 멤브레인 (MMMs)을 이용한
고성능 물/IPA 분리용 퍼베포레이션 연구)

Advisor: Prof. Kie Yong Cho

By
Gyeong Min Choi

A thesis submitted in partial fulfillment of the requirements
for the degree of

Master of Engineering

Department of Applied Chemical Engineering
(Major of Industrial Chemistry)
The Graduate School
Pukyong National University

February, 2025

Defective UiO-66 induced PVA-based Mixed Matrix Membrane (MMMs) for
High-Performance water/IPA Separation through Pervaporation

A dissertation
by
Gyeong Min Choi

Approved by:

Prof. Su Jong Chae

Prof. Jae Won Chang

Prof. Kie Yong Cho

21 February, 2025

Contents

Contents	i
List of Figures	iii
Abstract	vi

Chapter

1. Introduction	1
1-1. Metal-Organic Frameworks.....	1
1-2. Water/IPA Separation	3
1-3. Limitations of Mixed Matrix Membranes.....	5
1-4. Strategies for Enhancing Interfacial Interaction.....	7
Chapter 2. Experimental	9
2-1. Materials.....	9
2-2. Synthesis of Conventional and Defective UiO-66.....	10
2-3. Fabrication of free-standing PVA membranes.....	12
2-4. Fabrication of free-standing PUiO66 and PDUiO66 MMMs.....	13

2-5. Fabrication of Flat-sheet type XPUiO66 and XPDUiO66 MMMs...	14
2-6. Fabrication of hollow fiber type XPDUiO66 membranes.....	16
2-7. Chracterizations.....	17
2-8. Pervaporation test.....	19
Chapter 3. Results and Discussions.....	22
3-1. Synthesis and property evaluation of defective UiO-66 (DUiO66)...	22
3-2. Fabrication and Characterization of PVA based MMMs.....	33
3-3. Pervaporation performance of PDUiO66 MMMs.....	42
Chapter 4. Conclusions.....	61
Chapter 5. References	64
Chapter 6. Appendix.....	70
Acknowledgement.....	85

Fig.1. (a) schematic illustration of synthesis of defective UiO-66 (DUiO66) through control concentration of reactants and their comparative characteristics. (b) particle size distributions for conventional UiO66 and DUiO66. SEM images of (c1) UiO66 and (c2) DUiO66.

Fig.2. (a) PXRD patterns of UiO66 and DUiO66 normalized by α -alumina oxide. (b) Representative depiction of the structure and d -spacing values calculated from (111) plane for UiO66 and DUiO66. (c) Pore size distribution for UiO66 and DUiO66. (d) XPS C 1s narrow scan spectra of UiO66 and DUiO66. (e) Atomic ratio of C and O atoms relative to Zr derived from XPS.

Fig.3. (a) Zeta potential values of UiO66 and DUiO66 at pH 3.8 (1 mgmL⁻¹ in water, pH was measured after particle dispersion in DI water). (b) Solid-state ³¹P NMR spectra of TMPO-adsorbed UiO66 and DUiO66. (c) Solid-state ³¹P NMR spectra derived TMPO chemical and physical adsorption area of UiO66 and DUiO66. (d) Quantification of defects incorporated in UiO66 and DUiO66 structure and missing linker density per unit cell normalized by node residue. (e) Solution-state ¹H NMR of TMPO adsorbed UiO66 and DUiO66 in D₂O with NaOH (2M). (f) Normalized defect deficiencies of DUiO66 to UiO66 through TGA and ¹H NMR, respectively.

Fig.4. (a) FT-IR spectra and (b) XRD patterns of PVA, PUiO66, and PDUiO66 membrane. (c) UV-Vis spectra for PVA, PUiO66, and PDUiO66 membranes (inset: photographs of their individual membranes).

Cross-sectional SEM images (inset: surface images) of (d1) PVA, (d2) PUiO66, and (d3) PDUiO66.

Fig.5. (a) Illustration of interfacial interactions between PVA matrix and UiO66 or DUiO66 and their expected characteristics. (b) FT-IR spectra of PUiO66 and PDUiO66 membranes (inset: enlarged area around 480 cm^{-1}). (c) TGA curves of PVA, UiO66, DUiO66, PUiO66, and PDUiO66 under N_2 at a heating rate of $10^\circ\text{C min}^{-1}$. (d) DSC curves for PVA, PUiO66, and PDUiO66 membranes.

Fig.6. (a) Flux and separation factor plot for PVA, PDUiO66, and PUiO66 membranes measured at 70°C (feed composition: 80/20 (w/w) IPA/water) (b) Evaluation of PSI values and enhancement rates of PDUiO66 and PUiO66 membranes relative to pristine PVA membrane. (c) Swelling degree and (d) diffusion coefficient plots for PVA, PDUiO66, and PUiO66 membranes in each solution measured at 70°C . (e) Water isotherms for UiO66 and DUiO66 at 293K (inset: zoomed relative low pressure region). (f) UV-Vis spectra for UiO66 and DUiO66 dispersed solutions in water at a concentration of 1mgmL^{-1} after 1 week.

Fig.7. (a) Flux and separation factor plot for PDUiO66 membranes as a function of filler loading content tested at 70°C using 80/20 (w/w) IPA/water feed solution. (b) PSI values of PDUiO66 membranes with different DUiO66 filler loading (c) FE-SEM surface images of (c1) PDUiO66-4, (c2) PDUiO66-6, (c3) PDUiO66-8, and (c4) PDUiO66-10 (the sample name is denoted according to the DUiO66 filler loading) (d)

Tensile S-S curves of PDUiO66 with the different DUiO66 loading amount (inset: strength and modulus plot).

Fig.8. (a) Schematic illustration of the crosslinking process of the PDUiO66-2 membrane (after crosslinking, denoted XPDUiO66-2). (b) Flux and separation factor of XPDUiO66-2 with the variation of feed temperature at a feed solution of 80/20 (w/w) IPA/water. (c) Flux and separation factor of the XPDUiO66-2 membrane as function of feed composition measured at 70°C. (d) Long-term membrane performance of XPDUiO66-2 at 70°C

Fig.9. (a1) Illustration for fabrication of different membrane types and cross-sectional SEM images for different types of XPDUiO66-2: (a2) free-standing, (a3) flat-sheet, and (a4) hollow fiber (the photographs for all actula MMMs are displayed in (Fig.S9)). (b) Pervaporation performance plot for XPVA, flat-sheet, and hollow fiber type XPDUiO66-2 at 70°C using feed solution of 80/20 and 90/10 (w/w) IPA/water.

Fig.10. Comparison plot of (a) selectivity and (b) water in permeate vs. flux for XPVA and various types of XPDUiO66-2 membranes with different feed conditions measured at 70°C. (Red dot line: arbitrarily drawn polymeric membrane performance upper bound).

결합이 있는 UiO-66 을 도입한 PVA 기반 혼합 매트릭스 멤브레인
(MMMs)을 이용한 고성능 물/IPA 분리용 퍼베포레이션 연구

최경민

부경대학교 대학원 에너지융합소재공학과

요 약

금속 유기 골격체(Metal-Organic Frameworks, MOFs)는 넓은 표면적, 독특한 기공 구조 및 높은 변형가능성 등 다양한 특성으로 인해 가스 분리, 멤브레인, 촉매 등 다양한 분야에 활용되고 있다. 하지만, 고분자와의 상용성이 부족해 활용성이 떨어지는 단점이 있다. 특히 멤브레인에서 고분자와의 상호작용이 부족해 공극, 입자 뭉침 등 현상이 발생하고 이는 막의 기계적 안정성 및 성능의 저하를 유도한다. 본 연구에서는 MOF 입자에 의도적으로 결합을 유도해 고분자와 상호작용할 수 있는 작용기를 더 많이 형성함을 통해 고분자와의 상용성을 늘리려 한다. 이를 통해 고분자와 더 강한 상호작용을 형성하여 입자의 분산성을 향상시켜 멤브레인 내부의 공극, 입자 뭉침 등의 현상을 극복하여 멤브레인 안정성 및 성능을 향상시키고자 한다.

Defective UiO-66 induced PVA-based Mixed Matrix Membrane
(MMMs) for High-Performance water/IPA Separation through
Pervaporation

Gyeong Min Choi

Division of Applied Chemical Engineering
(Major of Industrial Chemistry)
Pukyong National University

Abstract

Metal-Organic Frameworks (MOFs) are widely used in various applications such as gas separation, membranes, and catalysts due to their high surface area, unique pore structure, and high tunability. However, the lack of compatibility with polymers remains a limitation in its practical application. Especially, in membranes, voids (sieve in the cage), particle agglomeration can be occurred by weak interfacial interactions between MOFs and polymers which is decreasing membrane's stability and performance. In this study, we aim to enhance the compatibility with polymers by intentionally inducing defects in MOF particles to generate more functional groups capable of interacting with polymers. This approach seeks to form stronger interactions with polymers, thereby improving particle dispersion, overcoming issues such as voids and particle agglomeration within the membrane, and ultimately enhancing membrane stability and performance.

Keywords: Mixed Matrix Membranes; Polyvinyl alcohol; Metal-organic frameworks;
Defect engineering; Interface engineering; Pervaporation



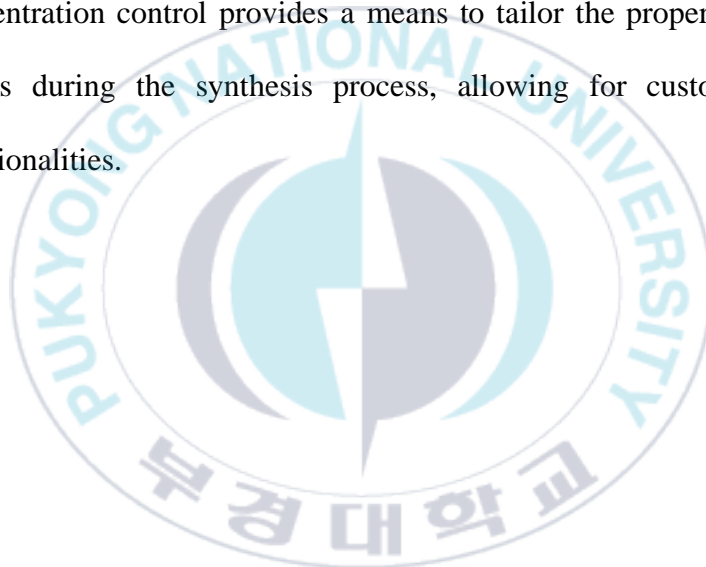
Chapter 1. Introduction

1-1. Metal-Organic Frameworks

Metal-organic frameworks (MOFs) are defined as one-, two-, or three-dimensional structures constructed through coordination bonds between metal nodes and organic ligands. MOFs exhibit exceptional properties, including a high specific surface area, unique pore structures, and remarkable tunability, making them suitable for applications in gas separation and storage, membranes, catalysis, and various other fields [1-4]. In particular, the high tunability and uniform pore structures of MOFs enable their extensive utilization across diverse applications [1-4].

However, unintended defects often form during the synthesis of MOFs, altering critical characteristics such as crystallinity, pore structure, interactions, and surface area [5-6]. These changes can significantly impact the performance of MOFs in specific applications. Therefore, controlling MOF defects is crucial for optimizing their functional properties. Various strategies, including

modulator adjustment, crystallization control, and post-synthetic modification (PSM), have been explored to regulate such defects [3-6, 7-10]. In most synthetic approaches, defect formation can be induced by adjusting the concentration of reactants. This concentration control provides a means to tailor the properties of MOFs during the synthesis process, allowing for customized functionalities.



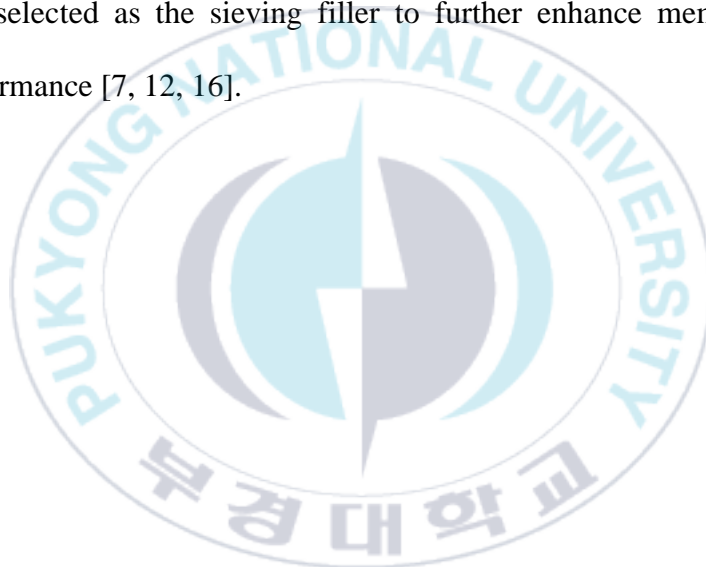
1-2. Water/IPA Separation

With the growth of the semiconductor industry and the increasing use of isopropyl alcohol (IPA) as a reactant, the need for efficient separation of IPA and water has become critical [11-12]. IPA is commonly used as a rinsing material for semiconductor wafers following the etching process. While distillation is the primary method employed to separate IPA from water in wastewater streams, the azeotropic nature of the mixture imposes significant limitations on the separation efficiency [13].

Mixed matrix membranes (MMMs) offer a promising alternative by incorporating porous fillers such as MOFs, COFs, and zeolites into polymer matrices to overcome the inherent performance limitations of polymer membranes. This approach enables separation with high purity beyond the azeotropic composition. Polyvinyl alcohol (PVA), a hydrophilic polymer containing abundant hydroxyl groups, exhibits strong interactions with water, making it an ideal candidate for such separation processes [14-15]. Based on these characteristics, this study aims to exploit the difference in diffusion rates between

IPA and water through PVA-based membranes to achieve high selectivity and permeability.

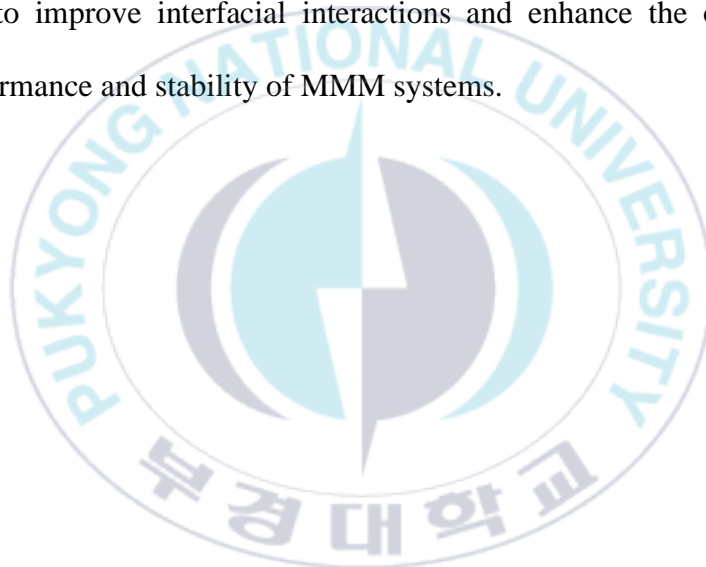
UiO-66, a metal-organic framework (MOF) with uniform pore sizes of approximately 6 Å and excellent thermal and chemical stability, was selected as the sieving filler to further enhance membrane performance [7, 12, 16].



1-3. Limitations of Mixed Matrix Membranes

To overcome the performance limitations of polymer membranes, porous materials such as MOFs can be utilized to amplify the difference in diffusion rates of substances traversing through the polymer's free volume. The specific pore sizes of MOF particles can induce a size sieving effect, thereby enhancing separation characteristics. However, in mixed matrix membrane (MMM) systems, weak interfacial interactions between MOF particles and polymers often result in a decline in membrane performance. These weak interactions hinder the polymer from adequately encapsulating the MOF particles, leading to the formation of voids at the interface. These voids create non-selective pathways, compromising the separation performance. Furthermore, insufficient dispersion of MOF particles within the polymer matrix causes particle aggregation. In such cases, the polymer fails to infiltrate the spaces between aggregated particles, forming non-selective regions that degrade membrane stability and performance.

To address these challenges, various strategies have been proposed, including reducing particle size to increase surface area, functionalizing either the MOF or the polymer, in-situ growth of MOF particles, and defect engineering [17-18]. These approaches aim to improve interfacial interactions and enhance the overall performance and stability of MMM systems.



1-4. Strategies for Enhancing Interfacial Interaction

To enhance the interfacial interactions between PVA and UiO-66 particles, intentional defects were introduced into the UiO-66 structure. This was achieved by controlling synthesis parameters such as the solvent and modulator quantities. As the amount of solvent decreased, the reaction system provided insufficient time for the formation of an ordered structure, leading to the creation of defect sites from a collision-theoretical perspective. Additionally, the modulator HCl influenced the ionization equilibrium of the metal precursor $ZrCl_4$ and terephthalic acid, thereby delaying the crystallization process.

Furthermore, Cl^- ions were reversibly adsorbed onto the open Zr sites, hindering the interaction between Zr and the terephthalic acid linker. This interference resulted in the formation of defects within the UiO-66 lattice. These defects allow hydroxyl groups to attach, enabling the formation of hydrogen bonds with the hydroxyl groups of PVA, thereby increasing interfacial interactions between the polymer and the particles [5].

By intentionally inducing such defects, a higher number of interaction sites are created, improving compatibility with polymers and addressing limitations of MMMs, such as particle aggregation and void formation. This approach contributes to overcoming the inherent challenges in MMM systems and enhancing their overall performance.



Chapter 2. Experimental

2-1. Materials

PVA (MW: 88,000–97,000 g mol⁻¹, 99% of hydroxyl degree) and dopamine hydrochloride (99%) were procured from Alfa Aesar. Zirconium chloride (ZrCl₄, 99.5%), glutaraldehyde (OHC(CH₂)₃CHO, 50%), and benzene-1,4-dicarboxylic acid (BDC, 99.5%) were purchased from Sigma Aldrich. Polyether sulfone (PES) was purchased from BASF Chemical. Other reagents, including n,n dimethyl formamide (DMF, 99.5%), N-methyl-2-pyrrolidone (NMP, 99.7%), hydrochloric acid (HCl, 35 ~ 37%), and isopropanol (IPA, 99.5%), were purchased from Dae-Jung Chemicals & Metals Co. All reagents were used as received without the further purification process.

2-2. Synthesis of Conventional and Defective UiO-66

Defect density controlled UiO66 and DUiO66 were synthesized by using solvothermal reaction following previously reported article [5]. Two separate solutions for ZrCl₄/HCl and BDC in DMF were prepared. ZrCl₄ (1.62 mmol, 0.38g) was dissolved in one-third of total volume of DMF (3.7 mL for DUiO66 and 15 mL for UiO66) with HCl (3.0 mL for DUiO66 and 1.5 mL for UiO66). The resulting solutions were sonicated and stirred at 80 °C until observing clear solution. BDC (2.25 mmol, 0.37g) was dissolved in two-third of total DMF volume (7.5 mL for DUiO66 and 30 mL for UiO66) at 80°C. ZrCl₄/HCl solution was poured into the BDC solution, and the reaction was conducted at 80°C for 24 hours under continuous stirring. After the process, the UiO-66 particles (UiO66 and DUiO66) were filtered and washed with DMF for 3 times (300 mL each) and ethanol for 2 times (300 mL each). The acquired UiO-66 powders (UiO66 and DUiO66) were dried at 70°C for 12 hours. Subsequently, the dried powders were activated by applying a

vacuum at 160°C for 12 hours and stored at the desiccator before usage.



2-3. Fabrication of free-standing PVA membranes

PVA (0.09 mmol, 8g) was dissolved in DI water (92 mL) with stirring at 90°C for 8 hours. The PVA solution was degassed by ultrasonic treatment until the bubbles are fully removed. Virgin PVA membrane was fabricated by knife casting method. the 8 wt% PVA solution was poured onto glass plate and then casted by using casting knife. The pristine PVA membrane was dried at 30°C for 12 hours and sequentially followed by thermal treatment at 80°C for 3 hours. The acquired MMMs were crosslinked using glutaraldehyde solution. The crosslinking solution was prepared following the process. 4 g of glutaraldehyde (0.04 mmol) was fully dissolved in water/IPA (100 mL, 90/10 w/w) with 1g of HCl as a catalyst. The fabricated MMMs was immersed in this solution at 50 °C for 1 hour. The crosslinked MMMs were washed with pure water and dried at 30°C for 12 hours.

2-4. Fabrication of free-standing PUiO66 and PDUiO66 MMMs

For fabricating PVA/UiO66 (PUiO66) and PVA/DUiO66 (PDUiO66) MMMs, the degassed PVA (0.09 mmol, 8g) was dissolved in DI water (80 mL) with stirring at 90 °C for 8 hours was conducted to fabricate MMMs as a polymer matrix. The synthesized UiO66 and DUiO66 powders (160 mg) were dispersed in 20 mL of DI water. After fully dispersion of UiO66 and DUiO66 fillers, they were mixed with the prepared PVA solution; the suspension was then stirred, and sonication was conducted for the homogenous mixture. The knife casting process was performed same with pristine PVA membranes and the after treatments. The thickness of the fabricated PUiO66 and PDUiO66 MMMs was estimated as ca. $30 \pm 5 \mu\text{m}$ regardless of the filler loading. The content of the fillers was varied from 2 wt% to 10 wt%.

2-5. Fabrication of Flat-sheet type XPUIO66 and XPDUiO66 MMMs

The support was fabricated following the process. 18 g of PES dissolved in 82 g of NMP at 80 °C. The dope solution was cooled down to room temperature and cast on the glass plate using a knife casting process by controlling the thickness to 100 μm. The casted PES support membrane was immediately immersed in the water bath and kept for overnight. The polydopamine coating was performed to overcome the poor affinity between the PES and PVA. The PES support was placed into the clean beaker after the pH was adjusted to 8.5 using tris HCl buffer solution. The 2 g of dopamine hydrochloride was added into the solution at 30°C for 2 hours. The polydopamine-coated PES membrane (D-PES) was washed with DI water and kept in ethanol before usage.

The flat sheet type thin MMMs were fabricated through the same knife casting procedure as the free-standing membranes. The

thickness was adjusted to 50 μm . crosslinking procedure was same with the XPVA membrane.



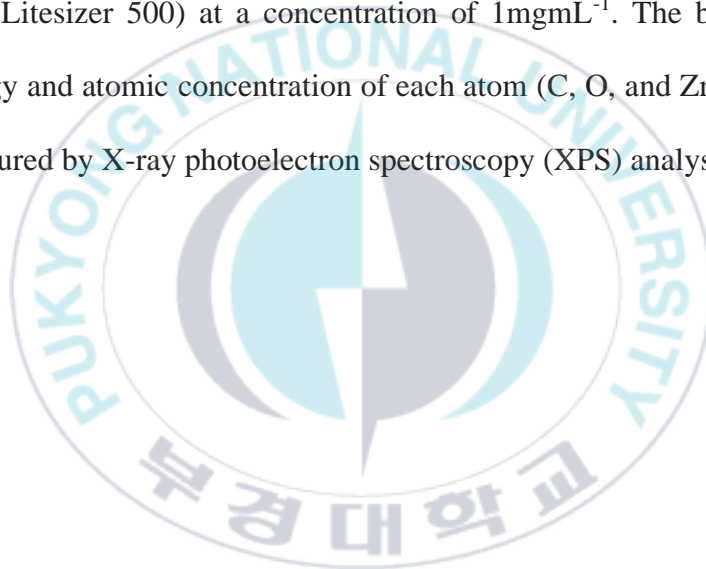
2-6. Fabrication of hollow fiber type XPDUiO66 membranes

Hollow fiber type thin XPDUiO66-2 was fabricated by a dip-coating process. The end of the alumina hollow fiber (AHF) support was capped with Teflon tapes and subsequently dipped into 8 wt% PVA solution (2 wt% DUiO66 loading) for 1 min and slowly put out. The membrane was fully dried at 30°C for 24 hours. The XPDUiO66-2 hollow fiber was crosslinked the same as the XPVA membrane.

2-7. Characterizations

Powder X-ray diffraction (PXRD) patterns were measured on a PANalytical diffractometer (X'Pert3-powder) operated at 45Kv and 40Ma with Cu-K α radiation ($\lambda = 1.5406 \text{ \AA}$) utilizing a diffracted beam monochromator. The values between $2\theta = 5^\circ$ and 40° were acquired. Thermal property analyses were performed by thermogravimetric analysis (TGA, SINCO TGA 1000) and DSC (TA Discovery DSC 25) at a heating rate of $10^\circ\text{C min}^{-1}$. TGA and DSC were measured under air state and N₂ state, respectively. Fourier transform infrared (FT-IR) spectra were acquired through Thermo Scientific Nicolet FT-IR system (iS10). The morphological images were investigated by utilizing TESCAN (MIRA 3LMH In-Beam Detector) Scanning electron microscope (FE-SEM) and optical microscope (OM, Carlo Zeiss, axiolab 5). The Brunauer-Emmett-Teller (BET) measurement was employed to analyze the N₂ adsorption-desorption isotherms and pore size distribution measured at 77 K. All samples were degassed at 60°C for 1h and 150°C for 2h under vacuum. ¹H NMR spectra were achieved by

dissolution of UiO66 or DUiO66 powder in D₂O with 2M NaOH. ³¹P NMR spectra were acquired in solid-state by FT-NMR 400 MHz (JEOL/JNM ECZ-400). Zeta potential and particle size distribution were measured by zeta potential and particle size analyzer (Anton Paar Litesizer 500) at a concentration of 1mgmL⁻¹. The binding energy and atomic concentration of each atom (C, O, and Zr) were measured by X-ray photoelectron spectroscopy (XPS) analysis.



2-8. Pervaporation test

The pervaporation tests were performed by using laboratory based equipments. The effective area of the membrane ($1.963 \times 10^{-3} \text{ m}^2$) was placed in a membrane cell consisting of two components. One of the membrane cells was linked with feed side (upstream side), and the other was connected to vacuum pump. The tests were performed for each membrane under various conditions including feed temperature and composition. The permeated solution was measured to define the composition ratio by using GC-MS (7090GC/5975 MSD). The separation factor, flux, and PSI values were calculated following the method provided by reported articles [19].

The separation factor (α) is defined as the follows:

$$\alpha_i = \frac{w_i^{permeate} / (1 - w_i^{permeate})}{w_i^{feed} / (1 - w_i^{feed})}$$

where w_i is the weight fraction of the compound i in the feed (w_i^{feed})

and the permeance ($w_i^{permeate}$).

$$\text{Flux } (J) = \frac{Q}{A \times t}$$

The flux (J) is determined by the weight of the permeate solution (Q) divided by the product of the membrane area (A) and operation time (t).

$$\text{PSI} = J \times (\alpha - 1)$$

Pervaporation separation index (PSI) is expressed as the product of flux and selectivity. This value represents overall pervaporation performance.

$$\text{Swelling Degree } (\%) = \frac{M_s - M_d}{M_d}$$

Swelling degree was calculated by the above equation, where M_s is weight of swollen membrane, M_d is the weight of dry membrane. Swelling degree of the membranes was measured in water, IPA and feed solution (Water/IPA, 20/80, w/w) at 70°C. The membrane were cut in 2 x 2 cm² pieces and weighed on the electronic balance. The cut membranes were immersed in each solution and kept for 24 hours to obtain equilibrium swelling state. Subsequently, they were

put out from the solution and wiped out the membrane surface and then weighed on the balance.



Chapter 3. Results and Discussion

3-1. Synthesis and property evaluation of defective UiO-66 (DUiO66)

Less defective conventional UiO-66 (UiO66) and more defective UiO-66 (DUiO66) were synthesized by controlling the volume of modulator (HCl) and solvent (DMF) (Fig. 1a). Due to the effect of hydrolysis delaying effect, interruption of non-participating materials, and chemical adsorption of Cl⁻ ion to the metal sites, the defects were introduced in UiO-66 structure. These defects create additional interaction sites within the MOF crystal structure, thereby enhancing interactions with polymers and specific molecules. The interaction enhanced by MOF defect might improve the interface, better dispersible properties, thermal, and mechanical properties compared to conventional UiO66.

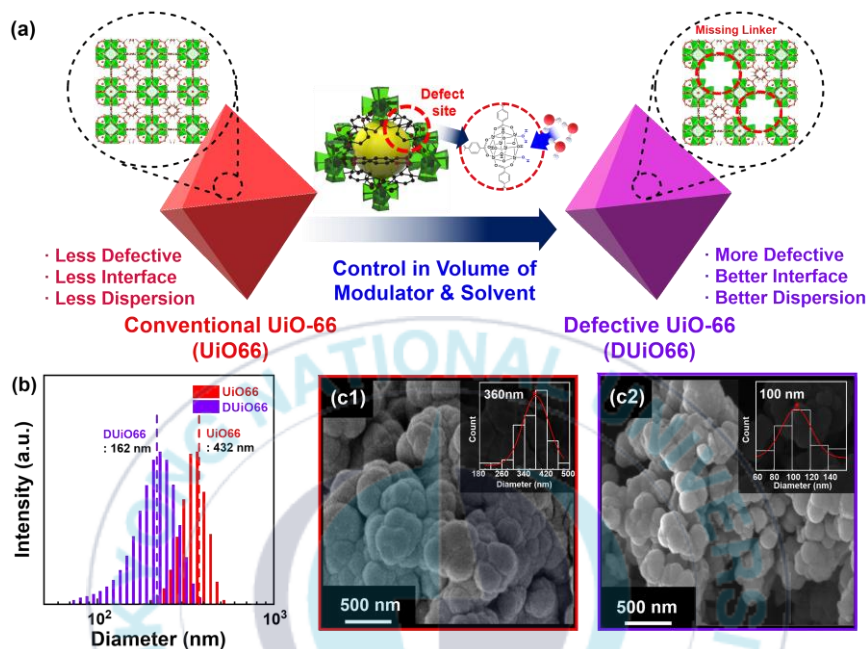


Fig.1. (a) schematic illustration of synthesis of defective UiO-66 (DUiO66) through control concentration of reactants and their comparative characteristics. (b) particle size distributions for conventional UiO66 and DUiO66. SEM images of (c1) UiO66 and (c2) DUiO66.

Particle size analysis was conducted through DLS analysis, resulting in the top point of ca. 432nm and ca. 162nm, respectively (Fig.1b). SEM analysis for UiO66 and DUiO66 was also performed to investigate the morphology and size difference, yielding spherical shapes for both of them and ca. 360nm (UiO66) and ca. 100nm (DUiO66) (Fig. 1c1 and 1c2) Both results from DLS and SEM were similar to each other. The HCl, the modulator of the synthesis, delayed the hydrolysis of $ZrCl_4$, and the controlled deprotonation of BDC. This phenomenon may help to explain the size variation in the synthesized UiO66 by adjusting the reactant concentration.

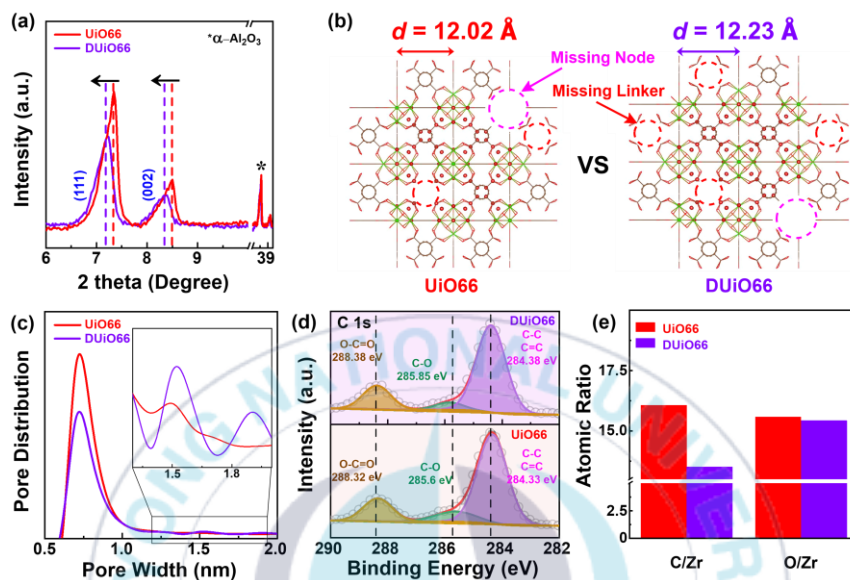


Fig.2. (a) PXRD patterns of UiO66 and DUiO66 normalized by α -alumina oxide. (b) Representative depiction of the structure and d -spacing values calculated from (111) plane for UiO66 and DUiO66. (c) Pore size distribution for UiO66 and DUiO66. (d) XPS C 1s narrow scan spectra of UiO66 and DUiO66. (e) Atomic ratio of C and O atoms relative to Zr derived from XPS.

The PXRD patterns for UiO66 and DUiO66 showed different crystalline properties when the peak intensity and position were aligned using α -alumina oxide (α -Al₂O₃) first peak at 37.75° (Fig.2a). DUiO66 showed relatively lower intensity and shifted to lower angle at two prominent peaks for (111) and (002) crystal plane compared to conventional UiO66 while simulated peak positions are similar to conventional UiO66 (Fig.S1). The peak intensity is highly related to crystallinity, which indicates DUiO66 has lower crystallinity than conventional UiO66. Based on the integrated area of XRD patterns, the normalized crystallinity of DUiO66 decreased compared to conventional UiO66, indicating a relative lower crystallinity of DUiO66 (Fig.S2). The PXRD peak position shifted to the lower angles for DUiO66, mainly associated with changes in crystal lattice which is mainly related to the increase of *d*-spacing. The value for DUiO66 (12.23 Å) was higher than the conventional UiO66 (12.02 Å) (Fig.2b). It can be affected by the electrical binding state in the frameworks changed by the defective structure such as missing linkers or nodes.

Pore structure and N₂ adsorption isotherm curves were measured (Fig.2c and Fig.S3). The main pore size at ca. 0.72nm for both UiO66 and DUiO66 was identical, the intensity for UiO66 was higher than DUiO66. The portion of larger pore size exhibited increasing trends in DUiO66 relative to those of UiO66. It can be related to an increase in defect density for DUiO66. The surface area and pore volume exhibited an almost retaining trend for both of UiO66 and DUiO66, exhibiting a marginal decrease compared to conventional UiO66 (Table S1). These decreases in surface area and pore volume may be due to the defect-induced pore structure change related to electrical binding state of the frameworks. These binding states were evaluated by utilizing XPS narrow scan for C 1s. XPS C 1s spectrum of DUiO66 exhibited marginal peak shift to the higher binding energy (Fig.2d). In addition, C 1s, O 1s, and Zr 3d spectrum were also acquired through XPS analysis, relative ratio of carbon or oxygen content to zirconium can offer significant evidence for identifying missing linker and node (Table S2). As depicted in Fig.2e, atomic ratio for C/Zr and O/Zr based on Table S2 showed

lower value for DUiO66 than UiO66. This result indicates that DUiO66 is more defective and C/Zr value for DUiO66 suggests that DUiO66 may have missing linker defect dominantly than missing node defects.



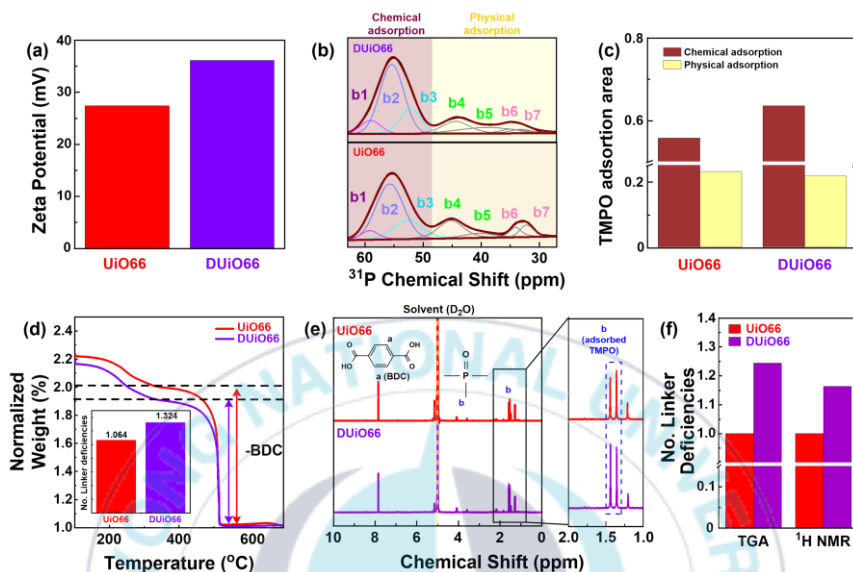


Fig.3. (a) Zeta potential values of UiO66 and DUiO66 at pH 3.8 (1 mg mL^{-1} in water, pH was measured after particle dispersion in DI water). (b) Solid-state ^{31}P NMR spectra of TMPO-adsorbed UiO66 and DUiO66. (c) Solid-state ^{31}P NMR spectra derived TMPO chemical and physical adsorption area of UiO66 and DUiO66. (d) Quantification of defects incorporated in UiO66 and DUiO66 structure and missing linker density per unit cell normalized by node residue. (e) Solution-state ^1H NMR of TMPO adsorbed UiO66 and DUiO66 in D_2O with NaOH (2M). (f) Normalized defect deficiencies of DUiO66 to UiO66 through TGA and ^1H NMR, respectively.

The identification of defect types was conducted through zeta potential and ^{31}P NMR. The zeta potential value of UiO66 and DUiO66 at pH after particles dispersion in DI water at a concentration of 1 mg ml^{-1} showed positive value 27.4 and 36.1 mV, respectively (Fig.3a). DUiO66 exhibited higher positive value due to the open metal site formed by missing linker defects. To support this result, ^{31}P NMR analysis was conducted. Trimethyl phosphine oxide (TMPO) was used as probe molecule which can be chemically adsorbed to the open metal sites formed by missing linker defects. Yin. J. et al discussed chemical and physical adsorption of TMPO. As suggested in previous article [20], DUiO66 showed increased chemical adsorption area relative to conventional UiO66 (Fig.3b). This result strongly suggests that missing linker defects were generated dominantly inside the DUiO66. In addition, the area of physical adsorption did not change as much as chemical adsorption, which indicates structural collapse did not happen while the defect formation (Fig.3c and Fig.S4). Based on these results, we can

conclude that the missing linker was primarily associated with DUiO66.

TGA tests for UiO66 and DUiO66 were performed to determine the amount of missing ligand defects in the synthesized UiO66 (Fig.3d). The weight loss caused by degradation of BDC was used to quantify the defect ratio. The weight loss was normalized based on the amount of residue left by the metal nodes, as it was previously confirmed to be a defect caused by the missing linkers. The ideal UiO66 MOF is composed of Zr_6O_8 node to BDC linker ratio of 1:6 in their unit cell. The ratio of Zr_6O_8 node to BDC for DUiO66 was decreased due to their missing linker defects, yielding defect density of 1.064 for UiO66 and 1.324 for the DUiO66. These findings indicate that DUiO66 has more missing linker sites relative to UiO66. To support this result, 1H NMR measurement for TMPO adsorbed UiO66 and DUiO66 was performed. The amount of adsorbed TMPO was qualified and exhibited high degree of TMPO adsorption for DUiO66 compared to UiO66 (Fig.3e). This result aligns with TGA result, indicating more missing linker sites were

formed inside the DUiO66. The combined outcomes from TGA and ^1H NMR analyses provide compelling evidence supporting the information that DUiO66 are having greater number of defects (Fig.3f). These results underscore the potential of DUiO66 as a promising materials on its defect-driven properties such as adsorption capabilities, interactions and subsequent performance. To qualify and provide accuracy of missing linker defects in DUiO66, acquired data of TGA and ^1H NMR measurement were normalized by using the number of missing ligand defect in UiO66. The relative degree of defects in DUiO66 exhibited higher defect content than UiO66 and the consistent trends were observed in both analysis techniques.

3-2. Fabrication and Characterization of PVA based MMMs

PVA membrane, PVA/UiO66 (PUIO66), and PVA/DUIO66 (PDUiO66) MMMs with 2 wt% filler loading were fabricated by knife casting method while the thickness was adjusted in 30 μm . The actual loading was calculated by using TGA curves, resulting in 1.85 ± 0.1 wt% for PUIO66 and *ca.* 1.69 ± 0.2 wt% for PDUiO66, respectively (Fig.S5 and Table S3). PVA was chosen as the polymer matrix due to its superior hydrophilicity and mechanical stability, facilitating enhanced polymer-water interactions. UiO-66 was known as one of the water-stable MOFs and it has 6 \AA of pore size, facilitating size-seiving between water (2.8 \AA) and IPA (~ 16 \AA).

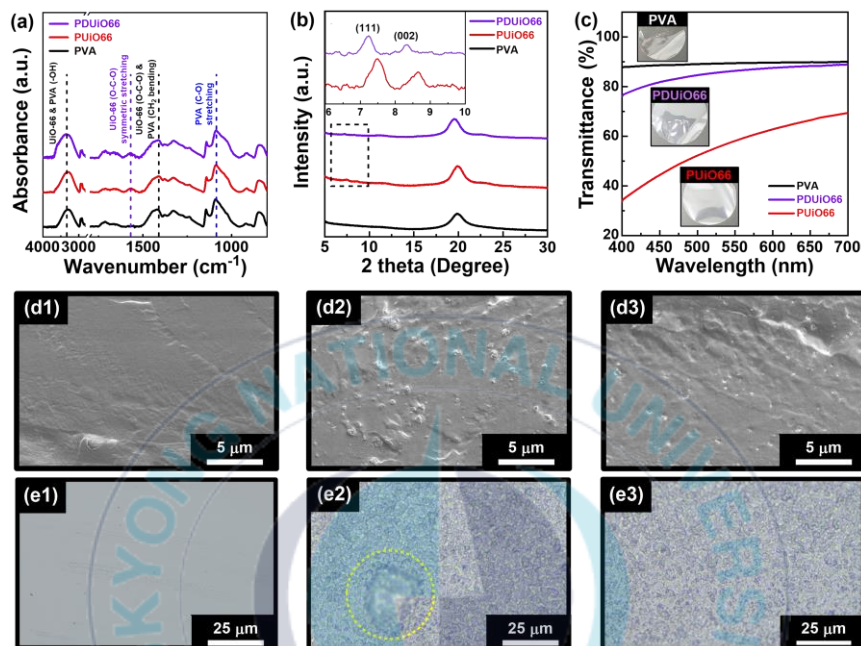


Fig.4. (a) FT-IR spectra and (b) XRD patterns of PVA, PUiO66, and PDUiO66 membrane. (c) UV-Vis spectra for PVA, PUiO66, and PDUiO66 membranes (inset: photographs of their individual membranes). Cross-sectional SEM images (inset: surface images) of (d1) PVA, (d2) PUiO66, and (d3) PDUiO66.

Successful fabrication of UiO-66 (UiO66 and DUiO66) into the PVA was confirmed by utilization of FT-IR spectra. The FT-IR spectra for PVA, PUiO66, and PDUiO66 exhibited the anticipated peaks (Fig.4a). C-O stretching ($1,144\text{ cm}^{-1}$), and -OH ($3,291\text{ cm}^{-1}$) peaks from PVA were detected in every membrane. The UiO-66 (UiO66 and DUiO66) fillers showed typical peaks; O-C-O asymmetric and symmetric stretching ($1,405$ and $1,590\text{ cm}^{-1}$). Those peaks are detected in PUiO66 and PDUiO66, indicating the UiO-66 particles are well incorporated with the PVA matrix. With the addition of UiO66 or DUiO66 fillers, -OH peak intensity around $3,400\text{ cm}^{-1}$ was increased (Fig.S6). PDUiO66 showed higher absorbance relative to PVA and PUiO66 membranes. To further identify the incorporation of PVA and UiO-66, XRD patterns were measured. XRD patterns for each membrane possessed the PVA crystalline peak at around 20° and exhibited typical UiO-66 peaks at around 7.35° and 8.50° , which correspond to (111) and (002) crystal plane, respectively (Fig.4b). It indicates that UiO-66 particles are stable after fabrication. The similar trends in peak

shifting were observed in XRD patterns for PUiO66 and PDUiO66. Interestingly, the PVA crystalline peak in PDUiO66 was shifted to the lower degree (19.5°) compared to PVA and PUiO66 (19.9°). This result can be attributed to the crystalline lattice changes by strong interfacial interaction between DUiO66 and PVA. The d-spacing value calculated by PVA crystalline peak exhibited highest value for PDUiO66 (4.54 \AA) relative to PVA (4.44 \AA) and PUiO66 (4.45 \AA). The fabricated membranes showed different transparency, exhibiting high transparency in PVA and PDUiO66 while very low transparency in PUiO66 despite the same loading content (2wt%). The PVA and PDUiO66 membrane showed high transparency of 89.4% and 86.3% respectively, while PUiO66 exhibited low transparency of 58.1% at 550 nm (Fig.4c). Those differences are caused by dispersion state of fillers in PVA matrix because of the light diffraction between the small and large particles. Through this result, DUiO66 may be more uniformly distributed in PVA matrix and have better interfacial interactions.

Cross-sectional SEM was employed to observe the morphologies of the neat PVA, PUiO66, and PDUiO66 membrane (Fig.4d1-d3). The PVA membrane showed a very smooth cross-sectional surface. The presence of filler was observed with few dots in both PUiO66 and PDUiO66. They do not show seive-in-the-cage morphology resulting in formation of non-selective paths, suggesting the preparing of the membranes were well fabricated without membrane defects. Optical microscopy (OM) has been performed to observe the surface morphology of each membrane (Fig.4e1-e3). The OM image of PVA showed a smooth surface. However, both PUiO66 and PDUiO66 exhibited relatively higher roughness which might be originated from the dispersion of nano-sized fillers in PVA matrix. Over 20 μm -sized fillers were found in PDUiO66 MMM, albeit not in the PDUiO66. While the average size of conventional UiO66 was 360 nm as discussed in Fig.1c1, it can not be observed without particle aggregation. These results are indicative that UiO66 and DUiO66 may have different dispersion state based on defect-derived different surface properties.

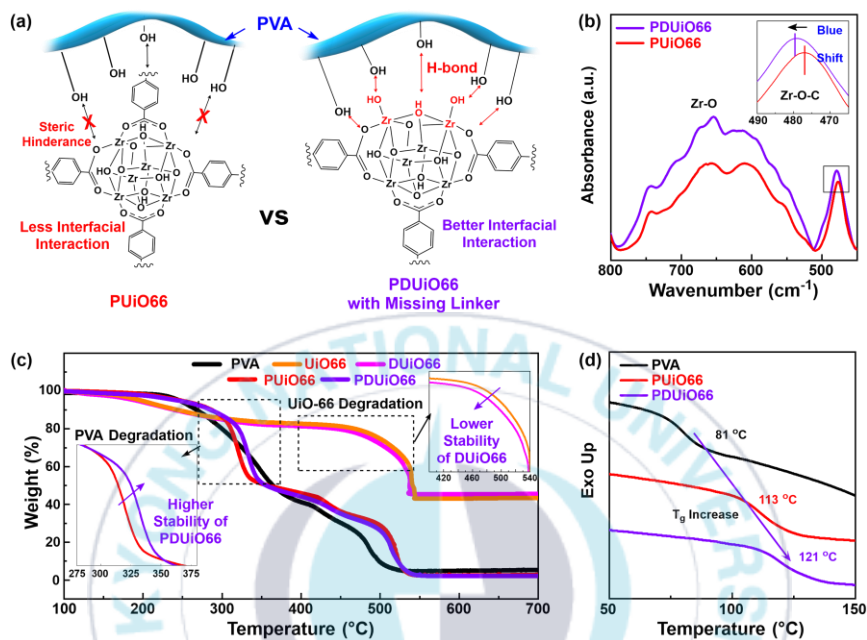


Fig.5. (a) Illustration of interfacial interactions between PVA matrix and UiO66 or DUiO66 and their expected characteristics. (b) FT-IR spectra of PUiO66 and PDUiO66 membranes (inset: enlarged area around 480 cm^{-1}). (c) TGA curves of PVA, UiO66, DUiO66, PUiO66, and PDUiO66 under N_2 at a heating rate of $10^{\circ}\text{C min}^{-1}$. (d) DSC curves for PVA, PUiO66, and PDUiO66 membranes.

Interfacial interactions between UiO-66 filler and PVA were identified through various analysis techniques including thermal, spectroscopical, and mechanical studies. The missing linker defects on UiO-66 can be saturated with hydroxyl group due to the charge neutralization as discussed in reported article [5]. These hydroxyl groups can enhance the interface between PVA and DUiO66 through the hydrogen bonding. This hypothesis for PDUiO66 facilitates significantly enhanced interactions among PVA, fillers and water molecules (Fig.5a). Better dispersion of DUiO66, reduced membrane defects, and enhanced properties can be achieved through these evidences.

This result was confirmed through FT-IR analysis, exhibiting a blue shift and higher intensity for Zr-O-C bonds at 654 cm^{-1} relative to PUiO66 (657 cm^{-1}) (Fig.5b). It explained more stiffness and quantity in PDUiO66 derived from better interfacial interaction between PVA and DUiO66 compared to PUiO66. In addition, the higher intensity of Zr-O bond around $449 - 509\text{ cm}^{-1}$ suggested that DUiO66 has more missing linker defects in their structure. Fig.5c

showed TGA curves for PVA, UiO66, DUiO66, PDUiO66, and PUiO66. The decomposition points of UiO66 and DUiO66 were compared and DUiO66 exhibited lower thermal properties than conventional UiO66 due to their high defect density. However, PDUiO66 membrane showed better thermal properties relative to PUiO66 which are attributed to enhance thermal stability.

The glass transition temperature of each membrane was measured through DSC study (Fig.5d). These curves can provide great evidences to understand for the interfacial interaction. When the particles formed a strong interaction with polymer matrix, it interrupted movement of amorphous region of polymer, resulting in increase of the T_g . The PVA showed 81°C; it was shifted to the higher temperature by the presence of UiO66 (113°C) and DUiO66 (121°C). The increase of T_g is related to increased interfacial interaction between UiO-66 fillers and PVA while PDUiO66 membrane exhibited higher increasing rate. To support this hypothesis, mechanical properties of the membranes were acquired through UTM. The tensile S-S curves for PVA, PUiO66, and

PDUiO66 showed the enhanced interaction between filler and polymer matrix (Fig.S7). The PDUiO66 membrane showed the highest stress and shortest strain relative to PVA and PUiO66 due to the strongest interactions between DUiO66 and PVA matrix. The tensile strength and modulus were calculated from the S-S curve. The PDUiO66 membrane showed highest values (33.6 and 9.8 Mpa, respectively) while the PVA and PUiO66 exhibited lower values (20.2 and 1.9 MPa for PVA, 26.6 and 6.4 MPa for PUiO66) compared to PDUiO66. The increase in mechanical properties of PDUiO66 also suggested that DUiO66 fillers could improve the interfacial interaction with PVA matrix.

3-3. Pervaporation performance of PDUiO66 MMMs

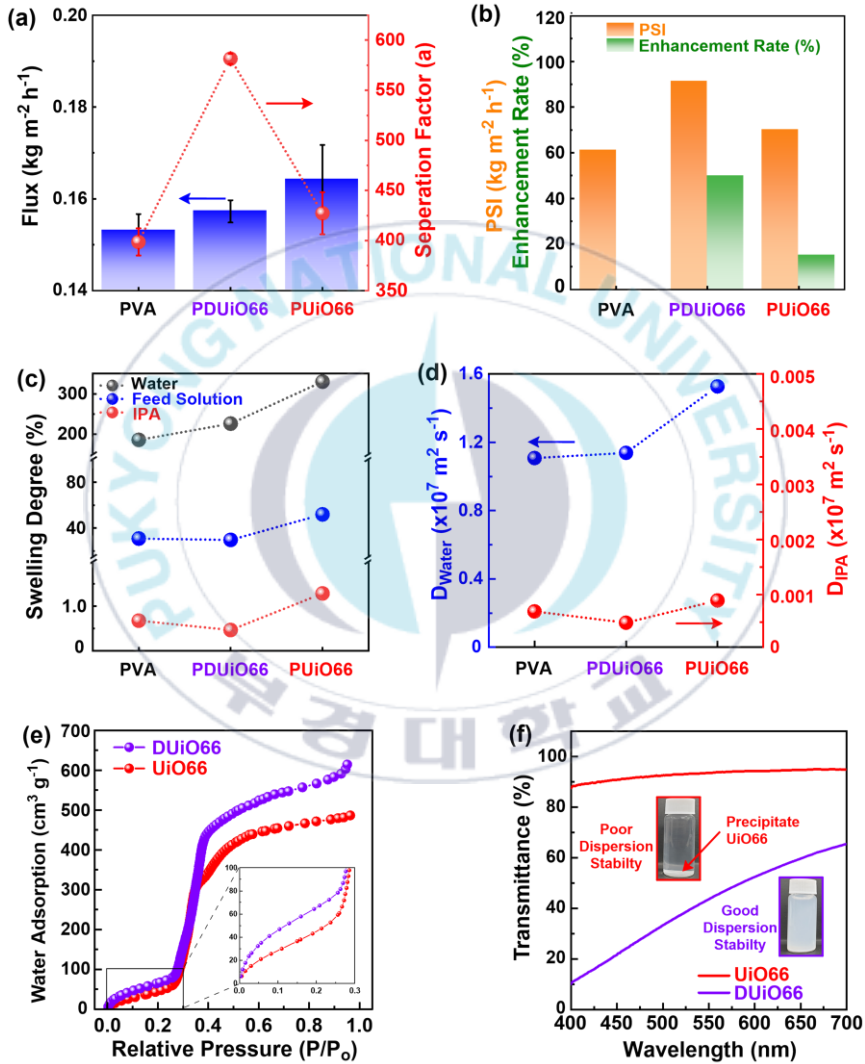
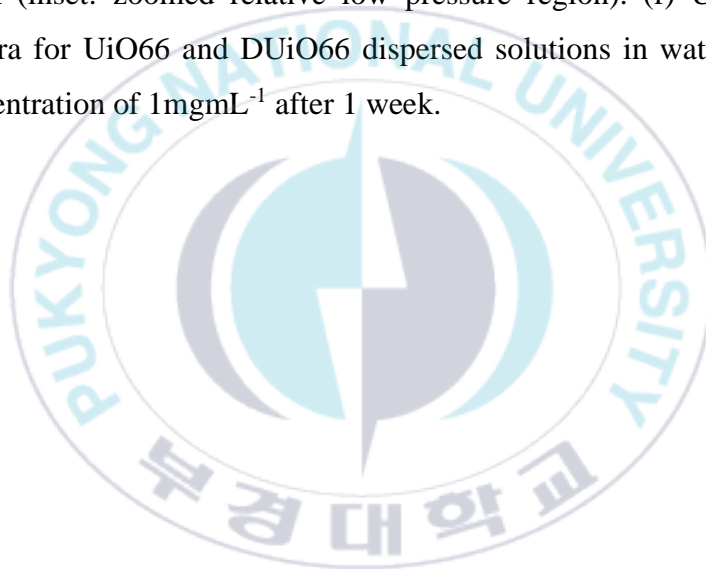


Fig.6. (a) Flux and separation factor plot for PVA, PDUiO66, and PUIO66 membranes measured at 70°C (feed composition: 80/20

(w/w) IPA/water) (b) Evaluation of PSI values and enhancement rates of PDUiO66 and PUiO66 membranes relative to pristine PVA membrane. (c) Swelling degree and (d) diffusion coefficient plots for PVA, PDUiO66, and PUiO66 membranes in each solution measured at 70°C. (e) Water isotherms for UiO66 and DUiO66 at 293K (inset: zoomed relative low pressure region). (f) UV-Vis spectra for UiO66 and DUiO66 dispersed solutions in water at a concentration of 1mgmL^{-1} after 1 week.



To evaluate the pervaporation performance, all the membranes were fabricated in the same conditions and the filler content for PUiO66 and PDUiO66 was consistent (2wt%). The impact of filler on the pervaporation performance at 70°C using an 80/20 (w/w) IPA/water feed solution. Pervaporation performance of the membranes can be effectively explained by the flux and the selectivity. The PDUiO66 MMM showed a slightly lower flux ($0.157 \pm 0.002 \text{ kg m}^{-2} \text{ h}^{-1}$) compared to PUiO66 MMM ($0.164 \pm 0.007 \text{ kg m}^{-2} \text{ h}^{-1}$) while exhibited higher flux than pristine PVA membrane ($0.153 \pm 0.004 \text{ kg m}^{-2} \text{ h}^{-1}$) (Fig.6a and Table S4). In contrast, the separation factor for PDUiO66 was measured as the highest value (581.4 ± 5.2) compared to PVA (398.7 ± 13.5) and PUiO66 (427.4 ± 21.0). The measurement was performed at least three times and the error range for each sample was provided in Fig. 6a. PDUiO66 exhibited the shortest error range compared to others, indicating the better stability and membrane reliability. This result might be also attributed to the filler effects on interfacial interaction. The pervaporation separation index (PSI) values for each membrane

were calculated to evaluate overall performance. The PSI value for PDUiO66, PUiO66, and PVA were calculated as 91.3, 70.0, 60.9 $\text{kg m}^{-2} \text{h}^{-1}$, the enhancement of PDUiO66 (49.7%) in PSI was 3.38-fold higher than PUiO66 (14.7%) (Fig.6b). It indicated the highest effectiveness of PDUiO66 in water/IPA separation. The DUiO66 is a more promising sieving material than the conventional UiO66. The difference in flux and selectivity can be described by the changes in solubility and diffusivity. The enhanced performance of PDUiO66 membrane can be explained by solution-diffusion model. The swelling degree of each membrane showed different behavior. The swelling degree revealed that the PDUiO66 increases solubility when it contacts with water, while its solubility in IPA showed relative decrease (Fig.6c). However, PUiO66 membrane exhibits as increasing trend in solubility for all solvents. In other perspectives, diffusivity, similar trends are observed. The enhancement in diffusion rate when in contact with water was acquired for PDUiO66 membrane, yet the diffusion rate to IPA was notably decreased (Fig.6d). In contrast, PUiO66 membrane displays an

increase in solubility and diffusivity for all solvents. The relative results of PUiO66 might be associated with particle aggregation due to limited dispersion properties and weak interfacial interaction with PVA chains compared to PDUiO66, as discussed in Fig.5.

The SEM analysis for the membranes supported our logics about filler aggregation. The PUiO66 membrane showed large aggregation compared to PDUiO66, which is consistent with the OM result for PUiO66 and PDUiO66 (Fig.4e). The DUiO66 fillers can be well-dispersed in the PVA matrix due to their enhanced interface derived from higher defect density. However, The SEM images of PUiO66 showed particle agglomeration which can produce the membrane defects resulting in non-selective pathways, contributing to reduced separation performance and enhanced permeability. The filler effects on the membrane pervaporation performance were investigated through water adsorption ability and dispersibility. The hydrophilic chemisorption was defined by the water adsorption at the initial relative low pressure range ($<0.2 P/P_0$), resulting in DUiO66 revealed the higher water adsorption properties

(Fig.6e). The saturated water adsorption for DUiO66 showed higher water adsorption capacity ($614.2 \text{ cm}^3 \text{ g}^{-1}$) compared to conventional UiO66 ($486.4 \text{ cm}^3 \text{ g}^{-1}$). Furthermore, after being dispersed in water for a week, UV-Vis measurement proved that DUiO66 particles had strong interactions with water molecules and revealed excellent dispersibility in water (Fig.6f). The well-dispersed DUiO66 solution showed opaque, while the UiO66 solution exhibited more clarity by the precipitation of UiO66 particles. These results described the high defect density of DUiO66 relative to the conventional UiO66. The presence of defects in DUiO66 was defined as missing linkers that can give hydroxyl groups on the metal nodes, which improve the interactions with water molecules and PVA matrix. These favorable interactions enhance the pervaporation performance by forming stronger bonds with water and facilitate interactions with PVA membrane.

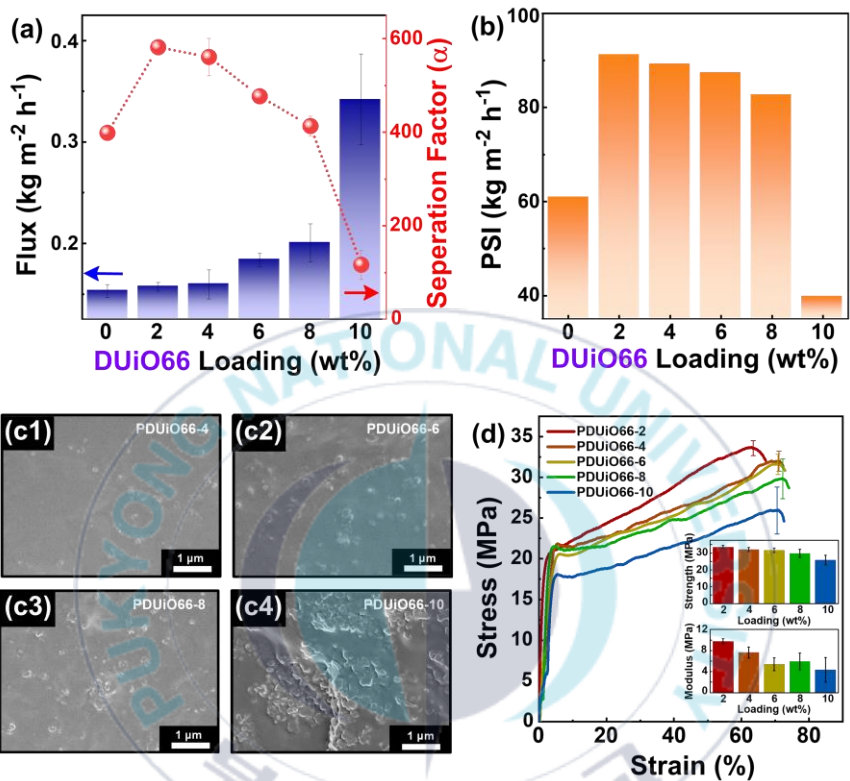


Fig.7. (a) Flux and separation factor plot for PDUiO66 membranes as a function of filler loading content tested at 70°C using 80/20 (w/w) IPA/water feed solution. (b) PSI values of PDUiO66 membranes with different DUiO66 filler loading (c) FE-SEM surface images of (c1) PDUiO66-4, (c2) PDUiO66-6, (c3) PDUiO66-8, and (c4) PDUiO66-10 (the sample name is denoted according to the DUiO66 filler loading) (d) Tensile S-S curves of PDUiO66 with the different DUiO66 loading amount (inset: strength and modulus plot).

Fig.7a depicts the impact of the DUiO66 filler loading content on PVA membrane performance. As the filler loading increases from 2 wt% to 10 wt% there is a gradual increase in total flux. However, beyond 2 wt% loading, the separation factor experiences a sudden decrease in PVA membrane. The possible reason for this changes is considered as the dispersion issue in the membrane over 2 wt% DUiO66 loading. At the 10 wt% of DUiO66 filler loading, the PSI value showed the lowest value ($39.7 \text{ kg m}^{-2} \text{ h}^{-1}$) compared to pristine PVA membrane ($60.9 \text{ kg m}^{-2} \text{ h}^{-1}$). The acquired SEM images to meticulous analysis, additional confirmation was sought in Fig.7c. The increase of DUiO66 filler loading revealed a notable trend: displayed inadequate aggregation and dispersion tendencies relative to PDUiO66-2. At the 10 wt% DUiO66 loading, more severe agglomeration was observed in PDUiO66-10 than others, resulting in significant increase of flux and a decrease in selectivity, PSI, and mechanical stability. The optimal DUiO66 filler loading content was determined as 2 wt% based on pervaporation performance. To explain above results, mechanical stability of the

membranes were investigated through UTM. As the DUiO66 loading content increased from 2 wt% to 10 wt%, the tensile strengths tend to decrease significantly, ranging from 33.58 MPa to 25.82 MPa. PDUiO66-2 showed the highest mechanical characteristics due to its proper loading and dispersity in the PVA matrix. These findings suggest dispersity issues generated over 2 wt% DUiO66 loading. Sadatnia et al. discussed PVA/ZIF-8 MMM, yielding a decrease with increase of filler content due to the heterogeneous dispersion state. It aligns with our suggestion that filler dispersion dependent mechanical property degradation. The optimized DUiO66 loading was determined based on PSI value of the membranes. This indicated that 2 wt% exhibited the highest effectiveness of PDUiO66 in water/IPA separation. The pervaporation performance for PDUiO66-2 showed the optimal dispersity and stable integration with PVA matrix. Hereafter, we performed further studies by utilizing PDUiO66-2.

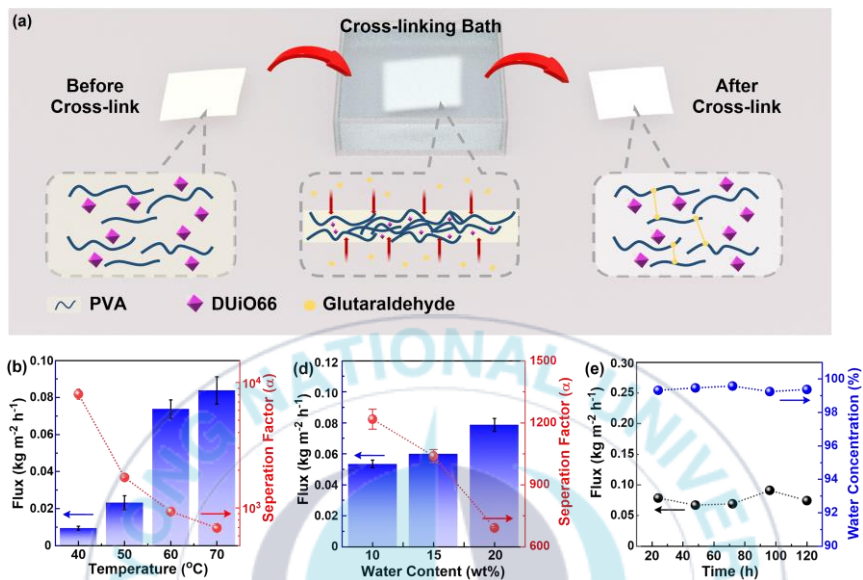


Fig.8. (a) Schematic illustration of the crosslinking process of the PDUiO66-2 membrane (after crosslinking, denoted XPDUiO66-2). (b) Flux and separation factor of XPDUiO66-2 with the variation of feed temperature at a feed solution of 80/20 (w/w) IPA/water. (c) Flux and separation factor of the XPDUiO66-2 membrane as a function of feed composition measured at 70°C . (d) Long-term membrane performance of XPDUiO66-2 at 70°C

A crosslinking reaction was performed on all membranes to enhance the membrane stability using glutaraldehyde, yielding crosslinked DUiO66/PVA (XPDUiO66) MMM, as depicted in Fig.8a. In general, a decrease in flux and increase in separation factor are commonly observed after the crosslinking reaction. Recognizing this tendency, a series of reliability tests were conducted. To measure the effect of feed temperature, pervaporation performance at different feed temperature was measured, allowing the determination of the molecular energy for each permeation component (Fig.8b and Fig.S8). When the temperature increases, molecular activity also increases, consequently leading to enhancing both permeability of each component. This enhancement of molecular activity contributed to decrease of selectivity and increase of permeability. Logarithmic Arrhenius plot of flux against temperature was plotted for each component mixture (Fig.S8). The activation energy of both IPA and water were calculated from the slope of the described graph. We observed that the activation energy for the permeation of water

(67.45 JK⁻¹ mol⁻¹) is lower than that of IPA (147.76 JK⁻¹ mol⁻¹). These results suggested that the PVA membrane state hinders diffusive transport in IPA relative to in water. It is understandable result in the common term from conventional pervaporation membranes. The favorable selectivity of the XPDUiO66-2 membrane towards water enhanced performance, especially at water feed composition of 10 wt%. As the water content increases 10 wt% to 20 wt%, the flux tend to increase due to the increased water content (Fig.8c). Its transportation effect and accessibility to the membrane surface facilitates the permeability of the feed solution. However, the separation factor exhibited decreasing trends due to high water concentrations in feed solution. As the proportion of water increases, the permeability of IPA interacting with water also increases, resulting in a decrease in selectivity. Long-term pervaporation test was also conducted, showing excellent membrane endurance and providing stability in fluxes and separation factors (Fig.8d). Those findings suggested that the optimized membrane, XPDUiO66-2, is well harmonized in the

membrane fabrication process and loading amount, resulting in high reliability from acquired results.



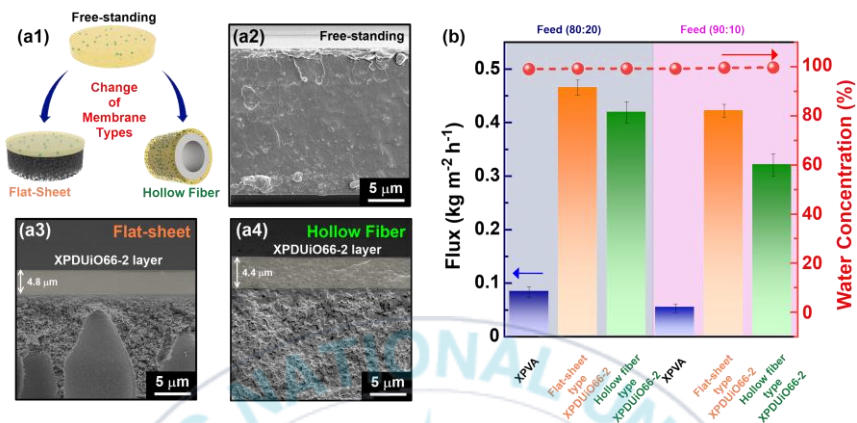


Fig.9. (a1) Illustration for fabrication of different membrane types and cross-sectional SEM images for different types of XPDUIO66-2: (a2) free-standing, (a3) flat-sheet, and (a4) hollow fiber (the photographs for all actula MMMs are displayed in (Fig.S9)). (b) Pervaporation performance plot for XPVA, flat-sheet, and hollow fiber type XPDUIO66-2 at 70°C using feed solution of 80/20 and 90/10 (w/w) IPA/water.

In our research, we comprehensively evaluated pervaporation performance at 70°C utilizing a feed solution of 80/20 and 90/10 (w/w) IPA/water based on different types of XPDUiO66-2 membranes to investigate proper types for high-performance pervaporation in combination of defective UiO66 (DUiO66) fillers and PVA matrix. The flat-sheet type and hollow fiber type XPDUiO66 membrane were fabricated and the thickness was measured through cross-sectional SEM images (Fig.9a1-a4). Those showed smooth surfaces and the selective layer (4.8 μm for flat sheet type and 4.4 μm for hollow fiber type) (Fig.9a3 and a4). This indicated that all XPDUiO66-2 MMM selective layers were well integrated on the support and reduction in its thickness compared to free-standing type (*ca.* 30 ± 5 μm reduction to *ca.* 4.5 μm) (Fig.9a2). Based on these results, we anticipated enhanced permeability by narrowing down the membrane thickness, albeit causing degradation in selectivity.

When comparing the pervaporation performance with different membrane types, both flat-sheet and hollow fiber type showed

significantly superior performance compared to the freestanding XPDUiO-66 regardless of feed composition (Table.S5). At a feed solution of 80/20 (w/w) IPA/water, flat-sheet type XPDUiO66-2 MMM showed the highest pervaporation performance (flux: $0.466 \pm 0.014 \text{ kg m}^{-2} \text{ h}^{-1}$, separation factor: 515.6 ± 9.8) compared to freestanding (flux: $0.084 \pm 0.009 \text{ kg m}^{-2} \text{ h}^{-1}$, separation factor: 691.6 ± 14.8) and hollow fiber type XPDUiO66-2 (flux: $0.419 \pm 0.020 \text{ kg m}^{-2} \text{ h}^{-1}$, separation factor: 558.1 ± 12.4) (Fig.9b). The flat-sheet and hollow fiber type XPDUiO66-2 exhibited 5.6 times and 5.0 times enhancements in flux compared to freestanding type, respectively. In addition, at a feed composition of 90/10 (w/w) IPA/water, enhanced separation factor (almost twice) was measured with degradation in flux when compared to the results evaluated at the 80/20 (w/w) IPA/water feed mixture. The acquired permeate showed ca.>99% water concentration regardless of feed composition, indicating high selectivity to the water.

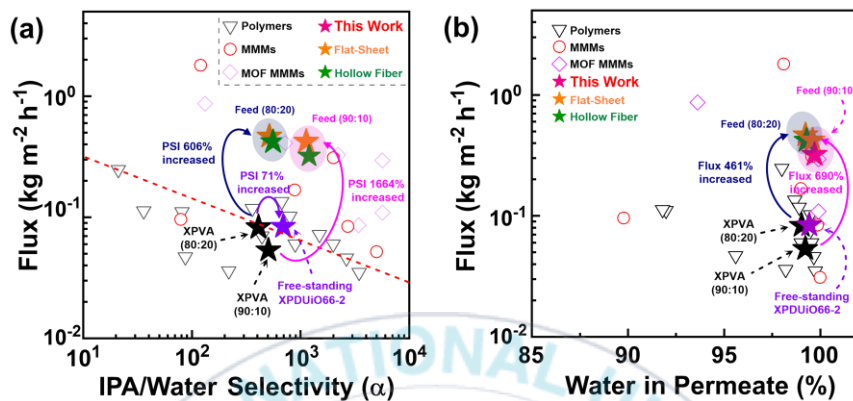


Fig.10. Comparison plot of (a) selectivity and (b) water in permeate vs. flux for XPVA and various types of XPDUiO66-2 membranes with different feed conditions measured at 70°C. (Red dot line: arbitrarily drawn polymeric membrane performance upper bound).

Furthermore, we relatively evaluated our results by comparing with reported state-of-the-art membranes for water/IPA separation (Fig.10a and 10b). Flat-sheet and hollow fiber type XPDUiO66-2 showed excellent pervaporation performance at a feed solution of 80/20 and 90/10 (w/w) IPA/water. These two types of membrane exhibited surpassing the upper bound (Fig.10a). Upon analyzing the selectivity data, it was found that the PSI value of free-standing XPDUiO66-2 increased by approximately 71% compared to XPVA at a feed solution of 80/20 (w/w) IPA/water. Notably, the flat-sheet XPDUiO66-2 exhibited significant improvements, with PSI values increasing by around 606% and 1,664% relative to XPVA at feed solutions of 80/20 and 90/10 (w/w) IPA/water, respectively. Moreover, the flat-sheet XPDUiO66-2 membrane demonstrated exceptional performance compared to previously reported membrane systems.

Additionally, when evaluating the permeate in terms of the moisture content ratio for the flat-sheet XPDUiO66-2, the flux increased by approximately 461% and 690% compared to XPVA at

feed solutions of 80/20 and 90/10 (w/w) IPA/water, respectively (Fig.10b). This result highlights the potential of flat-sheet XPDUiO66-2 membranes to achieve high selectivity and flux, surpassing state-of-the-art MMMs. The superior performance is attributed to the unique properties of the proposed DUiO66 (defective MOFs), including enhanced affinity for water, improved interface compatibility with PVA, better dispersion within the PVA matrix, and slightly adjusted crystal and pore structures. These attributes contribute to the development of stable and robust MMMs with substantially low thickness (approximately 4.5 μm) while providing enhanced solution and diffusion properties for water.

Chapter 4. Conclusion

This study was conducted to demonstrate the MOF's defects and changes in interaction and membrane performance derived from the defects. The defects were intentionally introduced by adjusting the concentration of the reactants through control of the amount of modulator and solvent. Identification and quantification study of UiO-66' defects were performed through utilization of various analysis techniques including SEM, XRD, XPS, NMR, Zeta potential, and TGA. We figured out DUiO66 (1.324) has more defect sites (missing linker defects) than conventional UiO66 (1.064). The defects incorporated with UiO-66 structure can affect the MOF properties such as interaction, pore structure, and molecule sorption. We anticipated these changes will lead powerful impact in various application fields. The pervaporation tests were conducted to prove the impact of these defects. PDUiO66 membranes were fabricated more uniformly without particle aggregation due to the enhanced interaction between PVA and DUiO66. Defects in

DUiO66 provides more interaction sites than conventional UiO66 which is contributing to the dimensional stability of the membrane and good interface. Free-standing type PDUiO66 membrane exhibits higher pervaporation performance than PVA and PUiO66. The enhancement of PDUiO66 (49.7%) in PSI was 3.38 times higher than PUiO66 (14.7%). The enhanced interaction between polymer and DUiO66 reduced membrane defects such as bypass and aggregation which may decrease the membrane performance by providing non-selective pathways. The membrane thickness was adjusted to reduce the resistance, and the thin selective layered MMMs were crosslinked for higher stability (XPDUiO66). The strengthened interface can help thin layered MMMs stable. Flat-sheet type and hollow fiber type XPDUiO66-2 (ca. 4.5 μm thickness) showed 5.6 times and 5.0 times higher flux than free-standing one at a feed solution of 80/20 (w/w) IPA/water while almost retaining their selectivity. Especially, the flat-sheet type XPDUiO66-2 acquired ca. 1,664 % enhancements in PSI relative to XPVA at a feed solution of 80/20 (w/w) IPA/water. This study successfully

proved MOF defects and how they affect the membrane interface and performance. In other words, this research described the relationship between MOF defects and membrane performance.



Chapter 5. References

- [1] H. Furukawa, K.E. Cordova, M. O’Keeffe, O.M. Yaghi, The chemistry and applications of metal-organic frameworks, *Science* (2013), 341, 1230444, <https://doi.org/10.1126/science.1230444>.
- [2] X.-Y. Han, D.-L. Pan, H. Chen, X.-B. Bu, Y.-X. Gao, H. Gao, Y. Tian, G.-S. Li, G. Wang, S.-L. Cao, C.-Q. Wan, G.-C. Guo, A methylthio-functionalized-MOF photocatalyst with high performance for visible-light-driven H₂ evolution, *Angew. Chem. Int. Ed.* 57 (2018) 9864–9869, <https://doi.org/10.1002/anie.201806077>.
- [3] K.Y. Cho, H. An, X.H. Do, K. Choi, H.G. Yoon, H.-K. Jeong, J.S. Lee, K.-Y. Baek, Synthesis of amine-functionalized ZIF-8 with 3-amino-1,2,4-triazole by postsynthetic modification for efficient CO₂-selective adsorbents and beyond, *J. Mater. Chem. A* 6 (2018) 18912–18919, <https://doi.org/10.1039/C8TA02797H>
- [4] B.R. Pimentel, A. Parulkar, E.-K. Zhou, N.A. Brunelli, R.P. Lively, Zeolitic Imidazolate Frameworks: Next-Generation

Materials for Energy-Efficient Gas Separations, *ChemSusChem* 7 (2014) 3202–3240, <https://doi.org/10.1002/cssc.201402647>.

[5] K.Y. Cho, J.Y. Seo, H.-J. Kim, S.J. Pai, X.H. Do, H.G. Yoon, S.S. Hwang, S.S. Han, K.Y. Baek, Facile control of defect site density and particle size of UiO-66 for enhanced hydrolysis rates: insights into feasibility of Zr(IV)-based metal-organic framework (MOF) catalysts, *Appl. Catal. B* 245 (2019) 635–647, <https://doi.org/10.1016/j.apcatb.2019.01.033>.

[6] Z. Fang, B. Bueken, D.E. De, R.A. Vos, Fischer, Defect-Engineered Metal-Organic Frameworks, *Angew. Chem. Int. Ed.* 54 (2015) 7234–7250, <https://doi.org/10.1002/anie.201411540V>.

[7] L. Valenzano, B. Civalleri, S. Chavan, S. Bordiga, M.H. Nilsen, S. Jakobsen, K. Petter Lillerud, C. Lamberti, Disclosing the Complex Structure of UiO-66 Metal Organic Framework: A Synergic Combination of Experiment and Theory, *Chem. Mater.* 23 (2011) 1700–1718, <https://doi.org/10.1021/cm1022882>.

- [8] J. Yin, Z. Kang, Y. Fu, W. Cao, Y. Wang, H. Guan, Y. Yin, B. Chen, X. Yi, W. Chen, W. Shao, Y. Zhu, A. Zheng, Q. Wang, X. Kong, Molecular identification and quantification of defect sites in metal-organic frameworks with NMR probemolecules, *Nat. Commun.* 13 (2022) 5112, <https://doi.org/10.1038/s41467-022-32809-9>.
- [9] O. Basu, S. Mukhopadhyay, S. Laha, S.K. Das, Defect Engineering in a Metal Organic Framework System to Achieve Super-Protonic Conductivity, *Chem. Mater.* 34 (2022) 6734–6743, <https://doi.org/10.1021/acs.chemmater.2c00654>.
- [10] Y.R. Lee, X.H. Do, K.Y. Cho, K.H. Jeong, K.-Y. Baek, Amine-Functionalized Zeolitic Imidazolate Framework-8 (ZIF-8) Nanocrystals for Adsorption of Radioactive Iodine, *ACS Appl. Nano Mater.* 3 (2020) 9852–9861, <https://doi.org/10.1021/acsanm.0c01914>.
- [11] A.F. Moslein, L. Don`a, B. Civalleri, J.-C. Tan, Defect Engineering in Metal–Organic Framework Nanocrystals: Implications for Mechanical Properties and Performance, *ACS*

Appl. Nano Mater. 5 (2022) 6398–6409,
<https://doi.org/10.1021/acsanm.2c00493>.

[12] B. Shan, S.M. McIntyre, M.R. Armstrong, Y. Shen, B. Mu, Investigation of Missing Cluster Defects in UiO-66 and Ferrocene Deposition into Defect-Induced Cavities, *Ind. Eng. Chem. Res.* 57 (2018) 14233–14241, <https://doi.org/10.1021/acs.iecr.8b03516>.

[13] M. Mujiburohman, W.B. Sediawan, H. Sulisty, A preliminary study: Distillation of isopropanol–water mixture using fixed adsorptive distillation method, *Sep. Purif. Technol.* 48 (2006) 85–92, <https://doi.org/10.1016/j.seppur.2005.07.025>.

[14] M.I. Baker, S.P. Walsh, Z. Schwartz, B.D. Boyan, A review of polyvinyl alcohol and its uses in cartilage and orthopedic applications, *J. Biomed. Mater. Res. Part B* 100B (2012) 1451–1457, <https://doi.org/10.1002/jbm.b.32694>.

[15] L. Liu, S.E. Kentis, Pervaporation performance of crosslinked PVA membranes in the vicinity of the glass transition temperature, *J. Membr. Sci.* 553 (2018) 63, <https://doi.org/10.1016/j.memsci.2018.02.021>.

- [16] S.-N. Wang, Z. Huang, J.-T. Wang, X.-F. Ru, L.-J. Teng, PVA/UiO-66 mixed matrix membranes for n-butanol dehydration via pervaporation and effect of ethanol, *Sep. Purif. Technol.* 313 (2023), 123487, <https://doi.org/10.1016/j.seppur.2023.123487>.
- [17] S. Japip, Y. Xiao, T-S. Chung, Particle-Size Effects on Gas Transport Properties of 6FDA-Durene/ZIF-71 Mixed Matrix Membranes, *Ind. Eng. Chem. Res.* 2016, 55, 35, 9507–9517, <https://doi.org/10.1021/acs.iecr.6b02811>
- [18] S.H. Park, K.Y. Cho, H-K. Jeong, Polyimide/ZIF-7 mixed-matrix membranes: understanding the in situ confined formation of the ZIF-7 phases inside a polymer and their effects on gas separations, *J. Mater. Chem. A*, 2020, 8, 11210-11217, <https://doi.org/10.1039/D0TA02761H>
- [19] P. Sampranpiboonb, R. Jiratananon, D. Uttapap, X. Fenga, R.Y.M. Huang, Pervaporation separation of ethyl butyrate and isopropanol with polyether block amide (PEBA) membranes, *J. Membr. Sci.* 173 (2000) 53–59, [https://doi.org/10.1016/S0376-7388\(00\)00351-3](https://doi.org/10.1016/S0376-7388(00)00351-3).

[20] Yin, J., Kang, Z., Fu, Y., Cao. W., Wang. Y., Guan. Hanxi., Yin. Y., Chen. B., Yi. X., Chen. W., Zhu. Y., Zheng. A., Wang. Q., Kong. X., Molecular identification and quantification of defect sites in metal-organic frameworks with NMR probe molecules. Nat Commun 13, 5112 (2022). <https://doi.org/10.1038/s41467-022-32809-9>



Chapter 6. Appendix

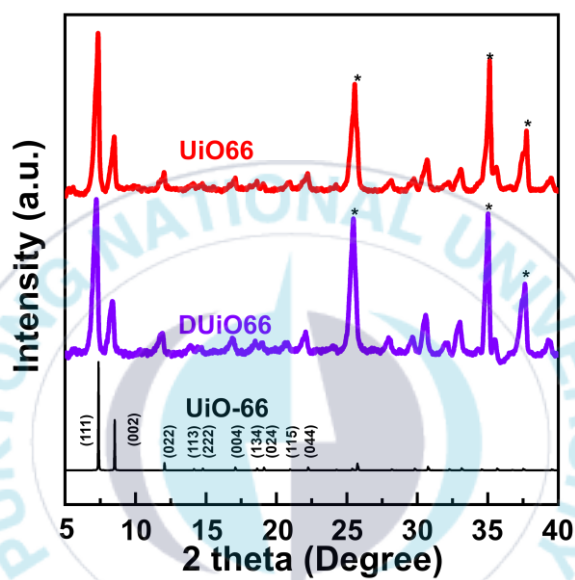


Fig. S1. PXRD patterns of simulated UiO-66, UiO66, and DUiO66. Each powder sample was mixed with α - Al_2O_3 in a weight ratio of 3:7 to normalize the intensity.

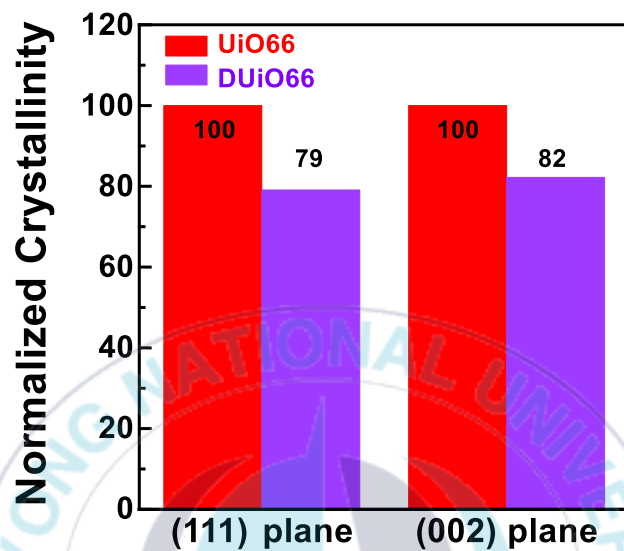


Fig. S2. Comparison of normalized crystallinity for each crystal plane of UiO66 and DUiO66.

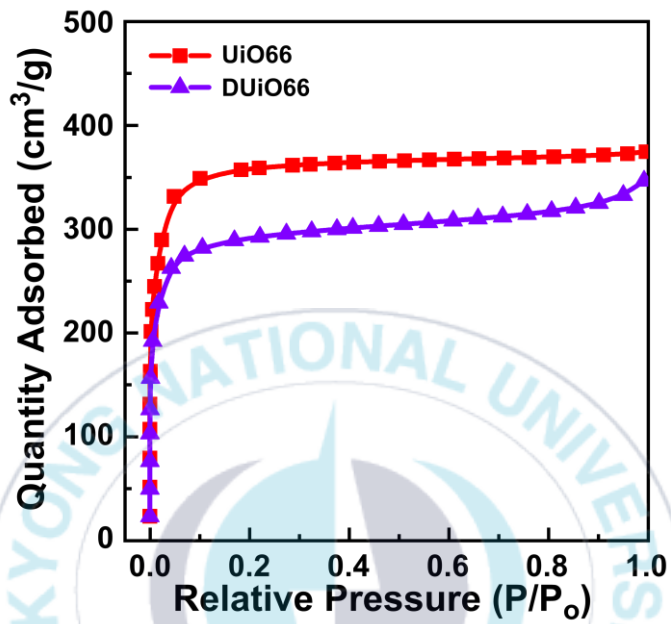


Fig. S3. N₂ adsorption isotherm curves for UiO66 and DUiO66 at 77 K.

Table S1. Surface area and pore volume of UiO66 and DUiO66.

	Surface area (m ² /g)	Pore Volume (cm ³ /g)
UiO66	1,834.06	0.703
DUiO66	1,571.12	0.671



Table S2. Summary of XPS scan data of UiO66 and DUiO66.

Sample		BE (ev)	Atomic (%)	Mass (%)
UiO66	Zr 3d	180.55	3.1	17.1
	C 1s	282.28	49.2	36.2
	O 1s	529.40	47.7	46.7
DUiO66	Zr 3d	180.48	3.3	18.2
	C 1s	282.38	45.1	32.4
	O 1s	529.45	51.5	49.3

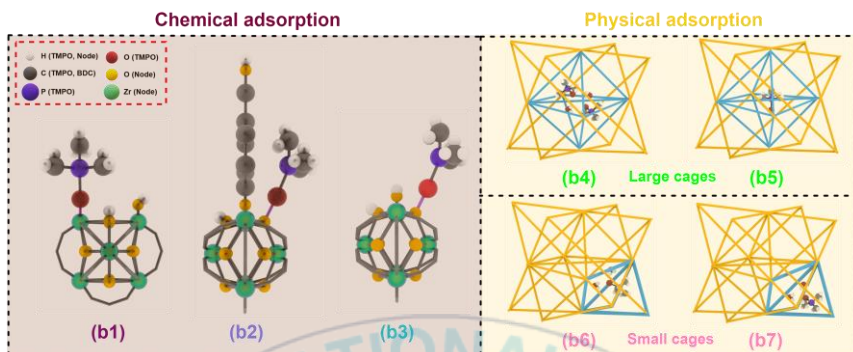


Fig. S4. Plausible structures for (b1-b3) chemical adsorption and (b4-b7) positions for physical adsorption in UiO-66.

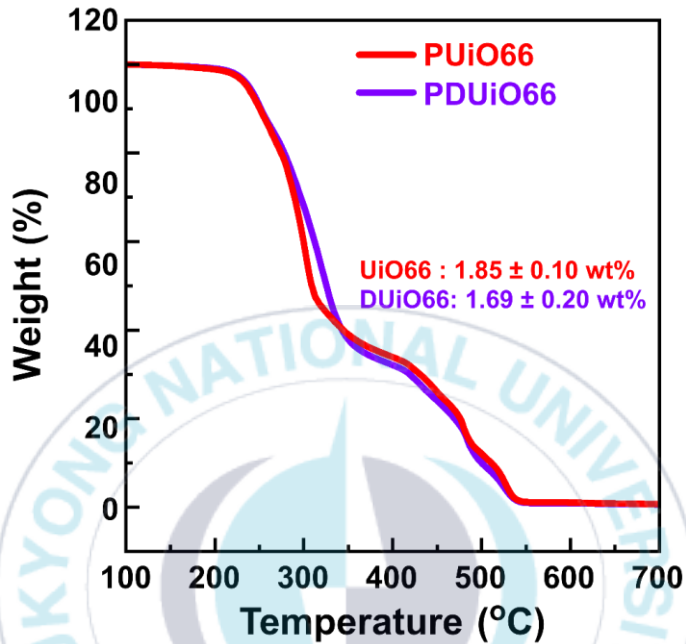


Fig. S5. TGA curves for PUiO66 and PDUiO66 MMMs (actual loading contents were calculated from residue) under air condition.

Actual loading concentration of UiO-66 was calculated by following the equation [1].

Method 1. Normalized to Structure

$$(1) M_w (\text{Zr}_6(\text{O})_4(\text{OH})_4(\text{L})_6) = 1,664 \text{ g mol}^{-1}$$

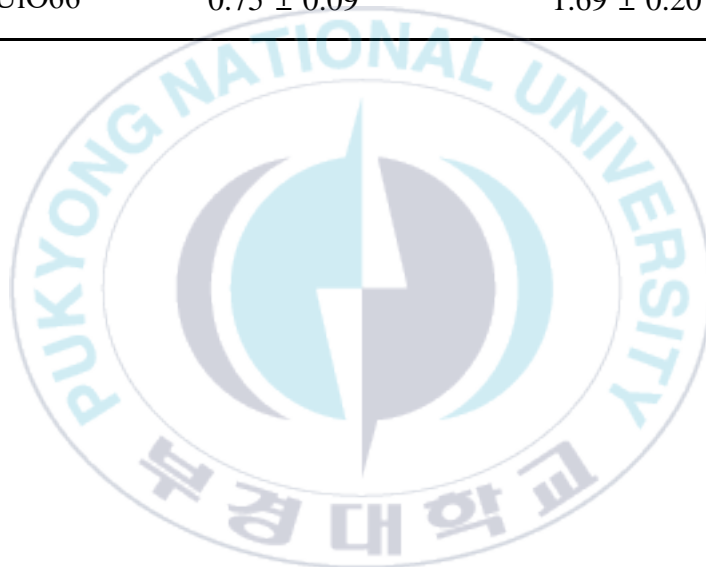
$$(2) M_w (6\text{ZrO}_2) = 739.34 \text{ g mol}^{-1}$$

$$(3) \text{mol}_{\text{Zr}} \text{ from Residue} = \frac{\text{Residual (wt\%)}}{M_w 6\text{ZrO}_2}$$

$$(4) \text{Loading concentration (wt\%)} = \text{mol}_{\text{Zr}} \times M_w (\text{Zr}_6(\text{O})_4(\text{OH})_4(\text{L})_6)$$

Table S3. Actual loading contents of DUiO66 and UiO66 fillers in PDUiO66 and PUiO66 membranes calculated from TGA curves.

Sample	Residual (wt%)	UiO-66 (wt%)
PUiO66	0.82 ± 0.04	1.85 ± 0.10
PDUiO66	0.75 ± 0.09	1.69 ± 0.20



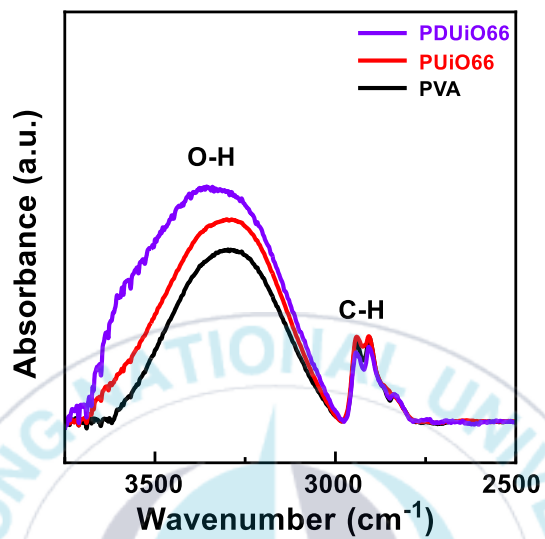


Fig. S6. FT-IR spectra of PVA, PUiO66, and PDUiO66 membranes.

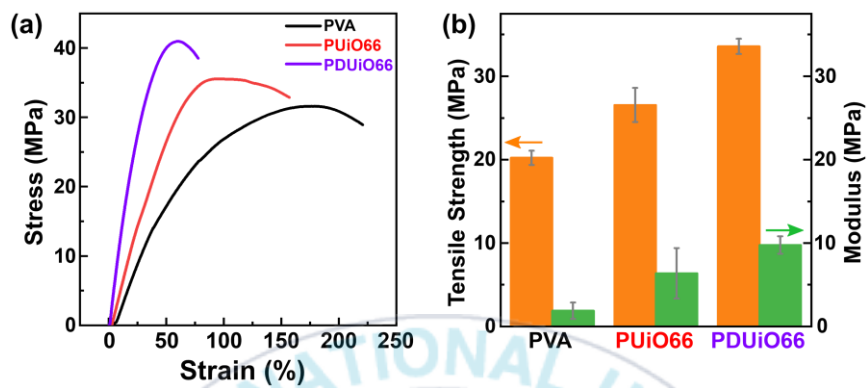


Fig. S7. (a) Tensile S-S curves and (b) tensile strength and modulus plots for PVA, PUiO66, and PDUiO66 MMMs.

Table S4. Pervaporation performance of tested membranes. Tests were conducted at 70°C.

Sample	Flux (kg m ⁻² h ⁻¹)	Separation factor (α)	PSI value (kg m ⁻² h ⁻¹)	Feed (IPA:Water)	Water permeates (%)
PVA	0.153 ± 0.004	398.7 ± 13.5	60.9	80:20	99.0
PUIO66-2	0.164 ± 0.007	427.4 ± 21.0	70.0	80:20	99.1
PDUiO66-2	0.157 ± 0.002	581.4 ± 5.2	91.3	80:20	99.3
PDUiO66-4	0.160 ± 0.014	560.5 ± 39.9	89.3	80:20	99.3
PDUiO66-6	0.184 ± 0.006	476.7 ± 6.8	87.5	80:20	99.2
PDUiO66-8	0.200 ± 0.019	413.2 ± 21.1	82.7	80:20	99.0
PDUiO66-10	0.342 ± 0.045	117.0 ± 31.3	39.7	80:20	96.7
XPVA	0.083 ± 0.010	409.6 ± 21.7	33.9	80:20	99.0
Free- standing type XPUiO66-2	0.083 ± 0.011	469.8 ± 18.7	39.1	80:20	99.2

Free-standing type XPDUiO66-2	0.084 ± 0.009	691.6 ± 14.8	57.9	80:20	99.6
Flat-sheet type XPDUiO66-2	0.466 ± 0.014	515.6 ± 9.8	239.5	80:20	99.2
Hollow Fiber type XPDUiO66-2	0.419 ± 0.020	558.1 ± 12.4	233.5	80:20	99.3
XPVA	0.053 ± 0.008	504.8 ± 12.9	28.5	90:10	99.2
Flat-sheet type XPDUiO66-2	0.422 ± 0.012	1125.8 ± 27.8	474.7	90:10	99.6
Hollow Fiber type XPDUiO66-2	0.321 ± 0.021	1195.3 ± 36.9	383.8	90:10	99.7

Table S5. Pervaporation performance of free-standing type XPDUiO66-2 according to water content in feed and temperature.

Flux (kg m ⁻² h ⁻¹)	Separation factor (α)	PSI value (kg m ⁻² h ⁻¹)	Feed (IPA:Water)	Water permeates (%)	Temperature (°C)
0.052 ± 0.002	1217.8 ± 48.6	175.3	90:10	99.9	70
0.060 ± 0.003	1039.7 ± 31.6	56.0	85:15	99.6	70
0.084 ± 0.004	691.6 ± 5.2	57.9	80:20	99.4	70
0.009 ± 0.001	8110 ± 754.7	76.6	80:20	99.9	40
0.023 ± 0.004	1750.7 ± 42.9	40.6	80:20	99.8	50
0.074 ± 0.005	934.9 ± 71.5	68.9	80:20	99.6	60
0.084 ± 0.007	691.6 ± 31.6	57.9	80:20	99.4	70

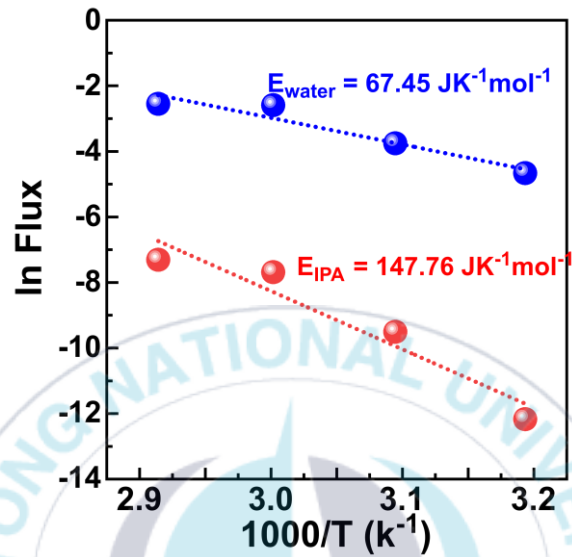


Fig. S8. Variation of $\ln \text{flux}_{\text{water}}$ and $\ln \text{flux}_{\text{IPA}}$ as a function of feed temperature at 80/20 (w/w) IPA/water.

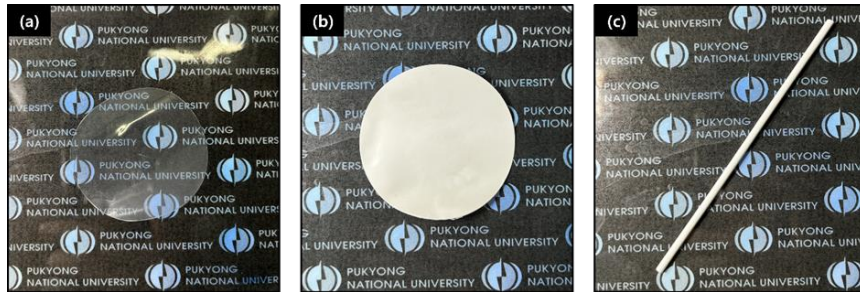
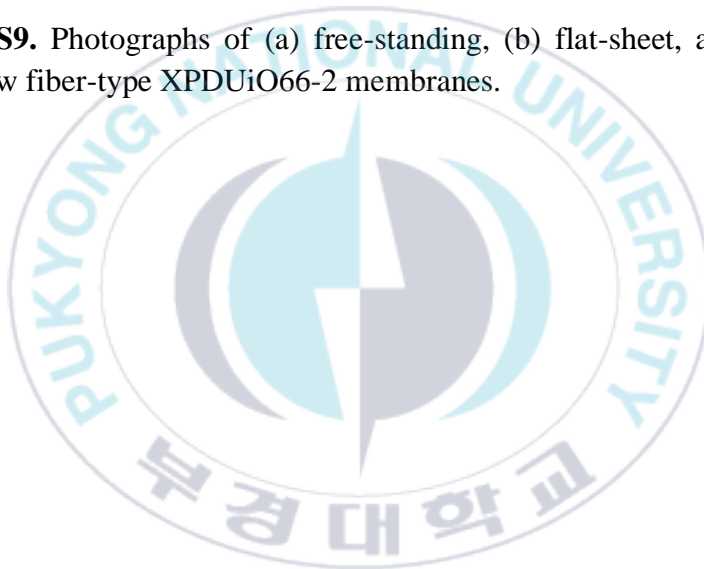


Fig. S9. Photographs of (a) free-standing, (b) flat-sheet, and (c) hollow fiber-type XPDUiO66-2 membranes.



Acknowledgment

I would like to express my gratitude to my supervisor, **Prof. Kie Yong Cho**. Over the past 2 years, your kind guidance and support provided lots of inspiration on my researches and life. The experience has greatly enhanced my capabilities as a researcher, including experiment design, execution, data analysis, and manuscript preparation, for which I am profoundly grateful.

Furthermore, I wish to convey my thanks to my seniors and colleagues, **Ho Jin Jeong, Manas Mandal, Hyeontae Shin, Young Je Kwon, Kaiyun Zhang, Ji Woo Bae, and Min Jeong Lee**. our collaboration and contributions were invaluable to the success of our work.

Lastly, I am deeply grateful to my family for their unwavering support, encouragement, and love, which have been a source of strength even in difficult times.

I hope that everyone who reads this paper finds happiness.

Thank you